2011

Development Of Theoretical Modeling And An Optical Characterization Systemfor Photodetectors In The 8-12 Îœm Wavelength Region

Jonathan Poe
North Carolina Agricultural and Technical State University

Development of Theoretical Modeling and an Optical Characterization System for Photodetectors in the 8-12 μm Wavelength Region

Jonathan Poe

North Carolina A&T State University

A thesis submitted to the graduate faculty

in partial fulfillment of the requirements for the degree of

MASTER OF SCIENCE

Department: Electrical & Computer Engineering

Major: Electrical Engineering

Major Professor: Dr. Shanthi Iyer

Greensboro, North Carolina

2011

School of Graduate Studies
North Carolina Agricultural and Technical State University

This is to certify that the Master's Thesis of

Jonathan Poe

has met the thesis requirements of
North Carolina Agricultural and Technical State University

Greensboro, North Carolina
2011

Approved by:

Dr. Shanthi Iyer Major Professor	Dr. Chung Yu Committee Member
Dr. Rexford Adelberger Committee Member	Dr. Clinton Lee Committee Member
Dr. John Kelly Department Chairperson	Dr. Sanjiv Sarin Associate Vice Chancellor for Research and Graduate Dean

Biographical Sketch

Jonathan Poe was born on May 30th, 1986 in Florida, USA. He received the Bachelor of Science degree in physics, computer information systems, and German from Guilford College in 2008. He is a candidate for the Master of Science degree in Electrical Engineering from North Carolina A&T State University. He is currently employed by the Massachusetts Institute of Technology and lives in Boston with his wife, Kathleen Kennedy.

Acknowledgements

I would like to express my gratitude to my adviser, Dr. Shanthi Iyer, for her guidance, support, and assistance throughout this thesis. I would also like to thank Dr. Jia Li for his daily assistance with the photoluminescence system. Thank you to my committee members, Dr. Chung Yu, Dr. Clinton Lee, and Dr. Rexford Adelberger. Special thanks to Dr. Adelberger for his guidance and support in the entirety of my scientific education thus far, but also with the theoretical work and reporting of this thesis. This thesis would not have been possible without the constant support and encouragement of my wife, Kathleen Kennedy.

This thesis was made possible by the support of ARO (Grant # W911NF-07-1-0577), under the direction of Program Manager Michael Gerhold.

Table of Contents

List of Figures

Abstract

A system was developed for characterizing molecular beam epitaxially grown III-V semiconductor materials and devices by measuring their photoluminescence and photoconductivity. The experimental system was tested on InSb substrates and a photoluminescence peak at 5.2 ± 0.1 μm was found, agreeing with published values. A photomask and photolithographic process for the fabrication of a P-I-N type photodetector device was developed, and a system was prepared for the measurement of the photoconductivity of the photodetector. A theoretical study was done for calculating the energy band structure of the semiconductor materials using the Kronig-Penney model. This model can predict the results of optical characterizations and act as a guide for the growth parameters to achieve a desired band structure. The methods in this thesis can describe, theoretically and experimentally, the band structure of the materials and devices grown in the lab.

CHAPTER 1

Introduction

Infrared detectors are often found in nature. An example is the sensilla organ of the jewel beetle, which allows it to detect forest fires from miles away[1, 2]. Other species such as snakes, fish and mosquitoes also have infrared detectors. The energy of an infrared (IR) photon is about 1 eV too low for the human eye to detect. Optoelectronic devices are being developed to allow us to detect IR radiation. These devices are called IR photodetectors and consist of a semiconducting film grown on top of a bulk substrate. After the film is grown by methods such as molecular beam epitaxy (MBE), the actual device is fabricated in a process called photolithography. Devices for detecting photons in the long wavelength infrared (LWIR) region, 8-12 μm, have many critical applications, including military aircraft-to-aircraft detection, missile defense, and space-based communications[3]. The LWIR region has a low atmospheric absorption window, making it particularly useful for sending and detecting signals passing through the atmosphere[4].

New material systems and device structures will continue to be invented to improve the power consumption, photoconductivity, durability, and other properties of photodetectors, while decreasing the cost and time of production. To make these improvements, a well-designed system, containing both theoretical and experimental pieces, is needed to characterize new materials and devices. In this thesis, we present such a system. A system was developed for measuring the photoluminescence of semiconductor materials and a theoretical model was developed to predict the energy gap given by photoluminescence. Additionally, a process was developed for fabricating a photodetector device and a system was developed for characterizing the photoconductivity of that device. The theoretical model developed uses the Kronig-Penney model[5] and the photodetector device design is a PIN-type[1] structure. The materials grown by MBE were GaSb, GaAs, InSb,

InSbN, and InGaSbN on GaSb, GaAs, and InSb substrates.

The most useful attribute of a photodetector is the frequency of light that it can detect. The energy of light is linearly related to its frequency by Plank's constant. Light, or electromagnetic (EM) radiation, comes in quantized packets of energy called photons. The energy of a photon determines its frequency and thus its place in the electromagnetic spectrum. The energy of photons emitted from a semiconductor depends on the allowed energy levels of the material. The allowed energy states for an electron in a material form bands when more than one atomic site become close together, that the Pauli exclusion principle broadens the individual atomic states. The forbidden energy states between these bands is called the band gap, or energy gap. The lowest energy band is called the valence band and is nearly full of electrons for a semiconductor. Above the valence band is a set of higher allowed energy bands spaced close together, called the conduction band.

In the MBE technique, various elements are released into a vacuum chamber and condensed onto the surface of a substrate, forming layers of film. The amount of each element used in the film and its layers contributes to an elemental composition, by which some percentage of one element used is compared to that of another element. The effective mass of an electron in a material depends on the material's composition and the thickness of each layer. Two or more semiconducting materials grown on top of one another in alternating layers is called a superlattice. The energy band structure of a superlattice is determined by the growth parameters, such as the thickness and elemental composition of the layers. Tailoring the growth process so that a specific band structure is achieved is called bandgap engineering and allows materials and devices to be designed for particular applications.

By knowing what compositions of elements and layer thicknesses to use in the growth of a thin film semiconductor, before the growth, that will yield a material with a specific band structure,

the speed and efficiency of a planned series of growths can be increased, while decreasing costs. Each growth can cost upwards of $1,000 and it is thus beneficial to be able to more accurately plan a growth schedule. If it were desired that a laser of a particular color or frequency be fabricated using a complex composition of compounds, by knowing what elemental composition and thickness of the layers to use in the growth, the bandgap can be accurately engineered to achieve the desired color or frequency. Similarly, a photodetector can be designed to operate in a certain frequency range by tailoring the growth process. Characterizing the grown materials and fabricated devices can verify theoretical calculations. Chapter 1 provides some high-level background information and Chapter 2 presents the theory of the Kronig-Penney model. Chapter 3 describes the details of experimental setups and photolithography, device design, and challenges faced. The results and discussion of results are presented in Chapter 4 and, finally, conclusions drawn and future work in Chapter 5.

CHAPTER 2

Theoretical Modeling

One method for theoretically calculating the allowed energy levels of a material is by applying the Kronig-Penney model to the material's electronic structure. In a crystalline material, the electrons are uniformly spaced throughout and the electric charge of each of these electrons creates a potential. By considering the material in just one dimension, the electrons form a periodic potential. The Kronig-Penney model is an idealized approximation of the shape of this potential, specifically a square-wave function, as shown in Figure 2.1[6], where a is the width of the peak of a square-wave (barrier), b is the width of the trough of a square-wave (well), V_o is the height of the square-wave (the potential), and the lattice constant is $d = a + b$. This repeating potential is given mathematically by

$$V(x) = \begin{cases} 0 & \text{for } 0 < x < a \\ V_o & \text{for } -b < x < 0 \end{cases} \tag{2.1}$$

It is the periodicity of this potential that yields electronic band structure. It is important to note

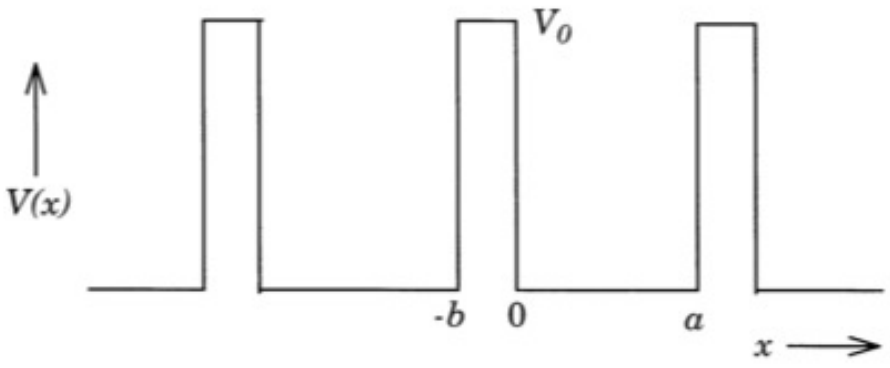

Figure 2.1. The Kronig-Penney potential approximation.[6]

that band structure cannot be achieved for a single well. There are more precise alternatives to the Kronig-Penney model for theoretically determining band structure, such as k.P perturbation theory and empirical pseudopotential, but the Kronig-Penney model is good enough for approximating band structure and guiding experimental growth, particularly at larger superlattice barrier widths[7].

Bulk material

Following the derivation given elsewhere[6], the time-independent, one-dimensional Schrödinger's equation is given as

$$-\frac{\hbar^2}{2m}\nabla^2 E(x) + V(x)\psi(x) = E(x)\psi(x) \tag{2.2}$$

where m is the mass of an electron, $V(x)$ is a periodic potential, such as that given in Figure 2.1, $\psi(x)$ is the wavefunction, and E is the electronic band energy. Equation 2.2 can be broken up into the two regions of equation 2.1, as

$$\frac{d^2\psi}{dx^2} + \frac{2mE}{\hbar^2}\psi = 0 \quad \text{for } 0 < x < a \tag{2.3}$$

$$\frac{d^2\psi}{dx^2} + \frac{2m\left(E - V_o\right)}{\hbar^2}\psi = 0 \quad \text{for } -b < x < 0 \tag{2.4}$$

The Born-von Karmen[8] boundary condition models the one-dimensional lattice as a ring of n atoms, which does not have a physical consequence when n is very large. By applying this boundary condition and a translational operator[6], and using Bloch's theorem[9] to solve for the wavefunction solution to equations 2.3 and 2.4, the final equation describing the energy of an electron in the one-dimensional lattice is given by

$$\frac{\beta^2 - \alpha^2}{2\alpha\beta}\sinh\left(\beta b\right)\sin\left(\alpha a\right) - \cosh\left(\beta b\right)\cos\left(\alpha a\right) = \cos\left(a + b\right)k \tag{2.5}$$

where

$$\alpha^2 = \frac{2mV_o}{\hbar}\frac{E}{V_o} = \frac{2mV_o}{\hbar^2}\epsilon \tag{2.6}$$

$$\beta^2 = \frac{2m\left(V_o - E\right)}{\hbar} = \frac{2mV_o}{\hbar^2}\left(1-\epsilon\right) \tag{2.7}$$

$$\epsilon = \frac{E}{V_o} \tag{2.8}$$

Equations 2.6, 2.7, and 2.8 yield

$$\frac{\beta^2 - \alpha^2}{2\alpha\beta} = \frac{1-2\epsilon}{2\sqrt{\epsilon}\sqrt{1-\epsilon}} \tag{2.9}$$

$$\beta b = \frac{b}{a}\left(\frac{2mV_o}{\hbar^2}\right)^{\frac{1}{2}} a\epsilon^{\frac{1}{2}} = rA\left(1-\epsilon\right)^{\frac{1}{2}} \tag{2.10}$$

$$\alpha a = \left(\frac{2mV_o}{\hbar^2}\right)^{\frac{1}{2}} a\epsilon^{\frac{1}{2}} = A\epsilon^{\frac{1}{2}} \tag{2.11}$$

where

$$r = \frac{b}{a} \tag{2.12}$$

$$A = a\sqrt{\frac{2mV_o}{\hbar^2}} \tag{2.13}$$

Substituting equations 2.9, 2.10, and 2.11 into equation 2.5 yields

$$\frac{\left(1-2\epsilon\right)}{2\epsilon^{\frac{1}{2}}\left(1-\epsilon\right)^{\frac{1}{2}}}\sinh\left[rA\left(1-\epsilon\right)^{\frac{1}{2}}\right]\sin\left(A\epsilon^{\frac{1}{2}}\right) + \cosh\left[rA\left(1-\epsilon\right)^{\frac{1}{2}}\right]\cos\left(A\epsilon^{\frac{1}{2}}\right)$$
$$= \cos\left[ka\left(1+r\right)\right] \quad \text{for } 0<\epsilon<1 \tag{2.14}$$

The left hand side of equation 2.14 is a function of ϵ, as

$$F(\epsilon) = \cos\left[ka\left(1+r\right)\right] \tag{2.15}$$

The allowed energy levels of the material can be predicted, theoretically, by plotting the left hand

side of equation 2.14 versus ϵ. Solutions to equation 2.15 exist only if the right hand side evaluates to between -1 and 1, because of the limits of the cosine function. Thus, by plotting the left hand side of equation 2.15 versus ϵ, the allowed states will have values between -1 and 1 and the forbidden states will have values < -1 or > 1. A Matlab function was written to search for the values where the left hand side of equation 2.15 is < -1 and > 1, to find the values of ϵ that correspond to the beginning and ends of energy gaps.

The effective electron mass (m) in InSb[10] is $0.014\, m_o$ and the lattice constant ($d = a + b$) is 6.479 Å. To choose the values for a, b, and V_o, notice that in equation 2.14, the hyperbolic functions do not oscillate. The argument of the regular trigonometric functions must be greater than 2π, as

$$\frac{2m\,V_o}{\hbar^2}a^2 > 4\pi^2 \tag{2.16}$$

$$Vo > \frac{2\pi^2\hbar^2}{a^2 m} \tag{2.17}$$

Thus, to get band structure, the values of a and V_o are coupled, as shown in equation 2.17.

So far, we have discussed analytical methods for applying the Kronig-Penney model, using transcendental equations. Another method that may prove useful in future development of this theoretical model is to numerically integrate Schrödinger's equation. The standard time-independent Schrödinger equation for one dimension, revised to accommodate a varying effective mass[11], is given as

$$\frac{-\hbar^2}{2m(x)}\nabla^2\psi(x) + V(x)\psi(x) = E\psi(x) \tag{2.18}$$

where E is the energy of the electron, whose eigenvalues are the allowed energies of the particle,

$m(x)$ is the effective mass of the particle as a function of distance in the superlattice, and $V(x)$ is a potential function. To use this in the well-known Runge-Kutta integration algorithm, equation 2.18 should be modified as

$$\nabla^2\psi(x) = -\frac{2m(x)}{\hbar^2}\left(E - V(x)\right)\psi(x) \tag{2.19}$$

The Kronig-Penney model specifies a simple square-wave potential function, written as in equation 2.1, but there are other functions that can be applied for higher accuracy, such as a parabolic function. Equation 2.18 can be integrated numerically using a Runge-Kutta algorithm, to find the allowed energy levels in a superlattice material. In each iteration of the program, the effective mass value can be changed according to the position in the layers. Also, the potential function can be set as a parabolic function or something more closely approximating the potential in a superlattice. A plot of the wavefunction, $\psi(x)$, will approach positive or negative infinity, depending on the value of energy, E. As the value of energy is increased, a change in sign in the wavefunction indicates the existence of the next allowed energy state. Then, the energy is decreased slightly, until the wavefunction becomes asymptotic with the horizontal axis. The energy level that makes this happen is a bound energy state. Further development is required of the numerical version of the program to accurately model a superlattice. The scope of this thesis is limited to a bulk material, InSb, for experimentally and theoretically testing a system developed for measuring photoluminescence.

Superlattice

In the future, the theoretical model should be extended to model a superlattice structure. A superlattice is a material structure in which thin layers of two or more types of semiconductors are alternately sandwiched on top of each other. In addition to the potential wells and barriers due

to the periodic potential from the electrons spaced uniformly in each of the semiconductor layers, in a superlattice structure there is another set of potential wells and barriers, from the potential of each layer as a whole. Characteristic of a superlattice is that tunneling must be taken into account, by which electrons can tunnel between coupled wells, from one material to another. This can happen when the potential barriers are very thin or the potential height (barrier height) is low. The fact that electrons can tunnel between materials, free to move through the superlattice, leads to the formation of continuous energy bands in the entire superlattice. The primary difference between superlattices and quantum wells is the tunneling of electrons. Even for multiple quantum wells, there is no interaction or tunneling of the electrons between wells, as is found with superlattices[12]. Instead, the allowed electron energies are quantized in quantum wells, confined to individual wells because of their larger barrier height or thickness. The band structure of a superlattice is comprised of minibands, where wavefunctions in the well overlap. The band structure and its minibands (smaller groupings of overlapping bands within the conduction and valence bands) can be set to desired levels by tailoring the growth parameters, specifically the thickness of the layers and the composition of the elements in each layer, which also determines the effective mass of an electron in each layer[13].

CHAPTER 3

Experimental Setup

Photoluminescence

Photoluminescence (PL) is an optical method for characterizing the physical properties of a semiconductor material. Laser light is focused onto the surface of a sample and absorbed in a process called photo-excitation, wherein the sudden excess of energy in the material causes electrons to go to a higher allowed energy state. When the electrons return to their equilibrium states, energy is released in the form of emitted light. The photons emitted are focused into a monochrometer. A grating inside of the monochrometer disburses the photons according to their frequency, before being absorbed by a photon detector. The photodetector records the intensity vs position of the dispersed beam, yielding intensity as a function of frequency. Change in voltage in the detector in response to the absorbed light is measured using an amplifier connected to a recording device, such as a computer. One of the important properties determined from PL is the band gap of the material[14]. The energy of the light emitted from the material is equal to the energy difference between the equilibrium and excited states. The frequency of the light is related to its energy by

$$E = h\nu \tag{3.1}$$

where the energy of the emitted photons, E, will have frequency, ν, linearly proportional to Planck's constant, h. Equation 3.1 predicts what energy a photon will need to have a particular frequency. A material's band structure depends on how it was grown and by tailoring a material's growth parameters to achieve a desired band structure, the difference between the electron's equilibrium and excited states can be set for a particular frequency of photon. The material growth

parameters can be guided theoretically with the Kronig-Penney model and then experimentally verified using PL.

A photoluminescence system was set up in the lab as shown in Figure 3.1. A laser was focused onto the surface of a sample and then a chopper was moved into the path of the laser to modulate the excitation to a particular frequency, adjustable by a digital controller connected to the chopper. The chopper used was a Stanford Research model SR540. The sample was mounted by mechanical means, using small metal clips, to the cold finger of an Advanced Research Systems cryostat. The chamber surrounding the sample is pumped down with a cryocompressor to keep the system and sample at a temperature of 10 K. The chamber consists of an inner, cylindrical shield and an outer shroud. The system is kept at low vacuum and temperature to limit absorption by other elements in the path of the radiation. The shroud has a quartz window through which the laser light was shown. The laser light that was reflected off of the sample was focused onto a set of off-axis, parabolically curved, elliptical-shaped, gold-plated mirrors, which in turn focused the laser light into an input slit of a Horiba iHR320 monochrometer. The mirrors were purchased from Edmund Optics. Gold plated mirrors were used because of their low absorption of IR radiation. The laser was focused into the monochrometer in the way as a guide for the PL radiation emitted from the sample, since we cannot see that with the naked eye. A grating inside of the monochrometer splits the light into its spectral components. The grating is adjusted by computer control so that one frequency at a time is focused into a detector at the output of the monochrometer. There are actually three gratings, #1 for the 1-4 μm range, #2 for the 4-7 μm range, and #3 for the 7-12 μm range. And three different detectors were used, a InSb detector, a GaSb detector, and a mercury cadmium telluride (MCT) detector, each liquid nitrogen-cooled to 77 K. The intensity of the light incident upon the installed detector is recorded by a computer with the help of a lock-in amplifier

from Stanford Research, model SR510.

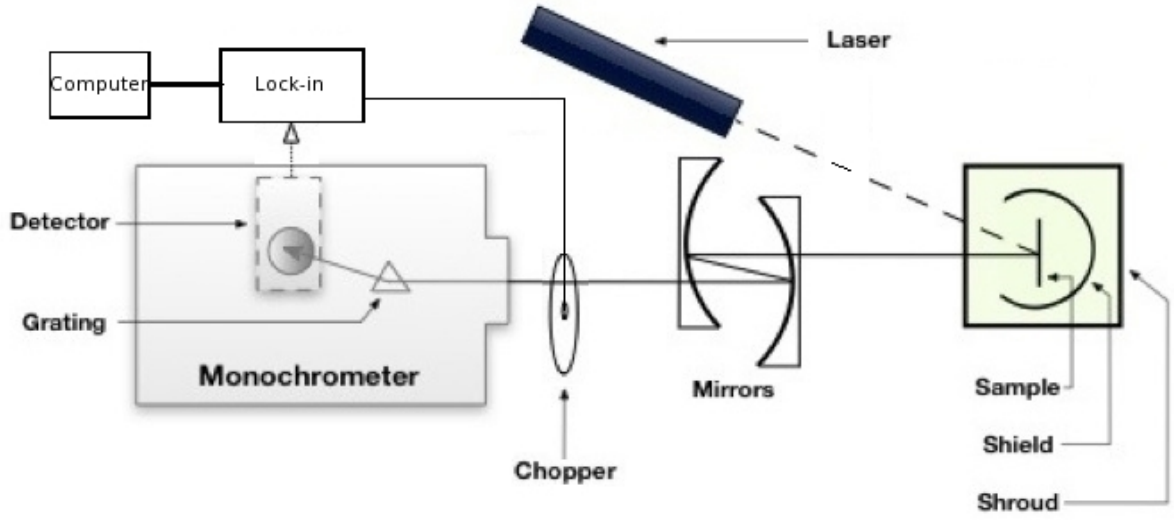

Figure 3.1. Schematic setup of the photoluminescence system.

A lock-in amplifier is used to detect very small ac signals. The intensity of the PL signal detected by the detector at the output of the monochrometer is often on the order of μV and there is frequently a high level of noise in the system, either from the cables used to connect the various components or from background radiation (local or cosmological). The lock-in technique is a method for measuring a small signal obscured by high noise levels. Fundamentally, a lock-in is a narrow band-pass filter tuned to the expected frequency of the chopper. This kind of filter rejects most unwanted noise, because the noise is not modulated to the chopper's frequency. The lock-in not only filters the signal, but amplifies it as well. There are many settings that can be adjusted on the lock-in amplifier to mitigate these sources of noise. The settings that were primarily used to mitigate noise and amplify a signal in this thesis were the sensitivity, pre-processing time, post-processing time, and phase. The sensitivity ranges from 1 nV to 500 mV. The pre-processing and post-processing time constants refer to two post demodulator low-pass filters. Each filter provides

6 dB/oct attenuation. The phase setting determines the phase shift between a reference oscillator in the lock-in and the input signal.

Noise is of constant concern in measurement of weak PL signals. There are many sources of noise, including Johnson noise, $\frac{1}{f}$ noise, vacuum flicker noise, and generation-recombination noise. These are all known as "intrinsic" noise sources. The other type of noise source is "non-essential" and can be eliminated with good laboratory practice. Typical, local non-essential noise sources are shown in Figure 3.2. Johnson noise arises from fluctuations of electron density in a resistor at a particular temperature. $\frac{1}{f}$ noise arises from fluctuations in the resistance of a current carrying resistor.

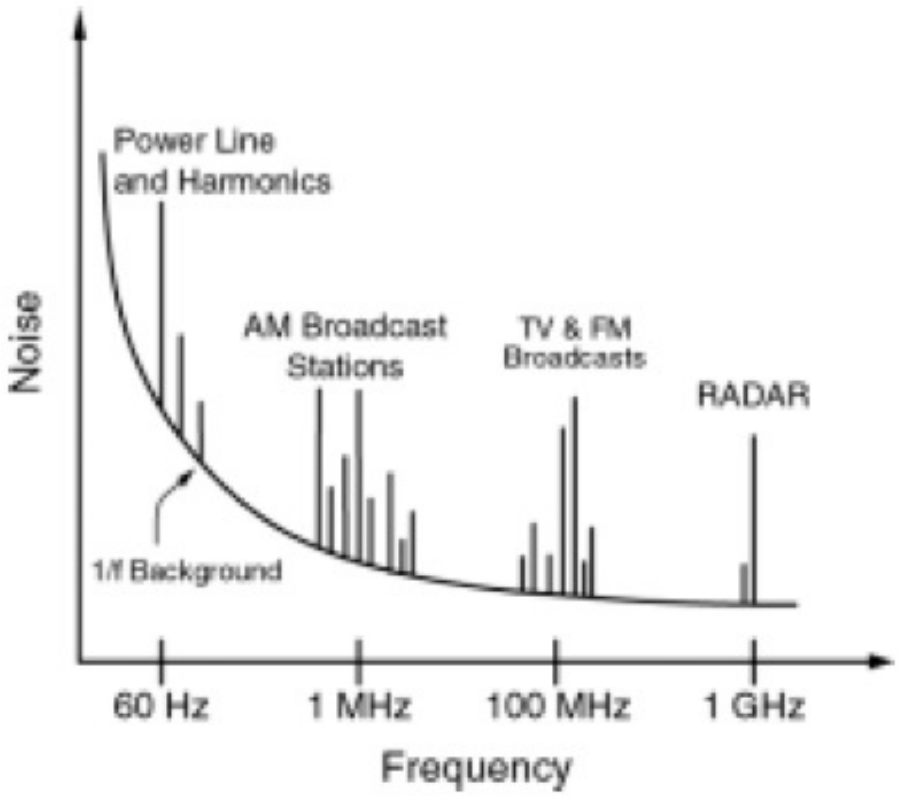

Figure 3.2. Typical, non-essential noise sources given in the Stanford Research lock-in manual.

Mounting the sample

We have previously used vacuum grease to mount samples to a flat sample holder. The problem with this approach is that vacuum grease is an insulative material. The sample itself will never reach the temperature of the sample holder. The shroud can reach a temperature of 50 K. While the shroud is in direct contact with the cryostat, the sample is in fact insulated from the cryostat. There are certain kinds of vacuum grease available, namely `Crycon` vacuum grease, which has copper or silicon powder mixed in the grease, so that the thermal conductivity increases. We were using Dow Corning High Vacuum Grease, which is a stiff, silicon lubricant used to lubricate glass, ceramic, and rubber pressurized valves. Still, the best option is to use mechanical means to adhere the sample to the sample holder. To mechanically attach a sample, Advanced Research Systems recommends drilling two small holes in the sample holder and inserting metal clasps to hold the sample. This has been implemented and all of our PL measurements in the future should use this method.

The sample holder is a small piece of copper that screws into the cold finger of the cryostat. It has a flat portion to which the sample is adhered. The first problem that we encountered in attempting to find a PL peak for a bulk substrate, was the presence of background radiation. We saw a broad peak centered at around 8 μm. The only problem was, when we turned the laser off, the peak persisted. We realized that this was going to be an important test for a PL peak: whether or not the radiation being detected was dependent on the sample being excited with a laser. Then, we removed the sample from the sample holder and got the same 8 μm peak, but the peak disappeared after removing the sample holder. We decided that the radiation must be coming from the sample holder itself. If it was not being excited with the laser, the only other kind of excitation in the system was thermal excitation. We recorded the radiation as the system was allowed to increase in

temperature, from 10 K back up to room temperature, and found that the radiation from the sample holder was temperature dependent. Blackbody radiation is a well-known temperature dependent type of radiation. The sample holder company suggested a nickel-plated sample holder, but we found this sample holder to only decrease the intensity of the μm peak by about 1/10 of that for the copper sample holder. This can be attributed to the fact that the nickel-plated sample holder still has copper at its core. Next, we tried boring out the middle of the copper sample holder at the point where the laser would be focused, since only radiation from that area of the sample holder should be directed at a spot on the parabolic mirrors that would be correctly focused into the monochrometer to get detected. This strategy also had very limited results, which can be attributed to the fact that the sample holder radiates isotropically and the inside of the shroud and shield are reflective and thus some of the radiation will make it to the focal point at the parabolic mirrors. It became clear that we were going to have to find some way of blocking the blackbody radiation.

Blackbody radiation

An ideal blackbody is theoretically possible, but more often found in nature as a graybody with varying degrees of ideality. This ideality factor is given the symbol ϵ and often referred to as emissivity. The emissivity constants for copper, polished copper and nickel-plated copper are 0.03, 0.033, and 0.37, respectively[15]. The Stephan-Boltzman Law can be revised to accommodate a graybody, as

$$P = \epsilon\sigma AT^4 \tag{3.2}$$

where ϵ is the emissivity constant, σ is Boltzmann's constant, A is the radiating surface area, and T is the temperature. It can be seen from equation 3.2 that the power of the radiation is proportional to the emissivity constant. When we record the radiation from a polished-copper sample holder

cooled to 10 K, we see a peak at 8 μm. The radiation for a nickel-plated copper has the same peak at 8 μm, but with slightly less intensity, attributed to the underlying copper. When we take out the sample holder and record the radiation from an empty shroud, we get zero intensity for all wavelengths in our measurement range (4-12 microns). However, there is some small amount of noise in this zero-measurement, which may explain why we do not see even a very small peak from the underlying copper that exists in the nickel-plated copper shroud. We attempted next to place an absorbing material in between the sample holder and the sample, such that the peak from the sample holder would be shielded from leaving the exit window of the shroud.

Absorbing wafers

We collected spectra for GaAs, GaSb, and InSb bulk wafers, shown in Figure 3.3. All of these spectra were recorded with no laser shining on the sample, nor any visible light entering the shroud window. A black curtain enclosed the optical bench and the overhead lights were turned off. The intent here was to see how effective the various substrates that we will be using for our samples absorb the radiation from the sample holder. From these data, it appears that none of the wafers absorb the radiation, but actually amplify the intensity of the radiation. In decreasing order, the intensities were recorded for GaSb, InSb, and GaAs. Figure 3.3 shows the cases when: no sample holder is attached to the cryostat; copper sample holder attached, but with no sample on it; nickel-plated holder, no sample; and the copper sample holder with GaSb, GaAs, and InSb bulk wafers, respectively. Each of the bulk wafer curves appear to have identical characteristics to that of the copper sample holder.

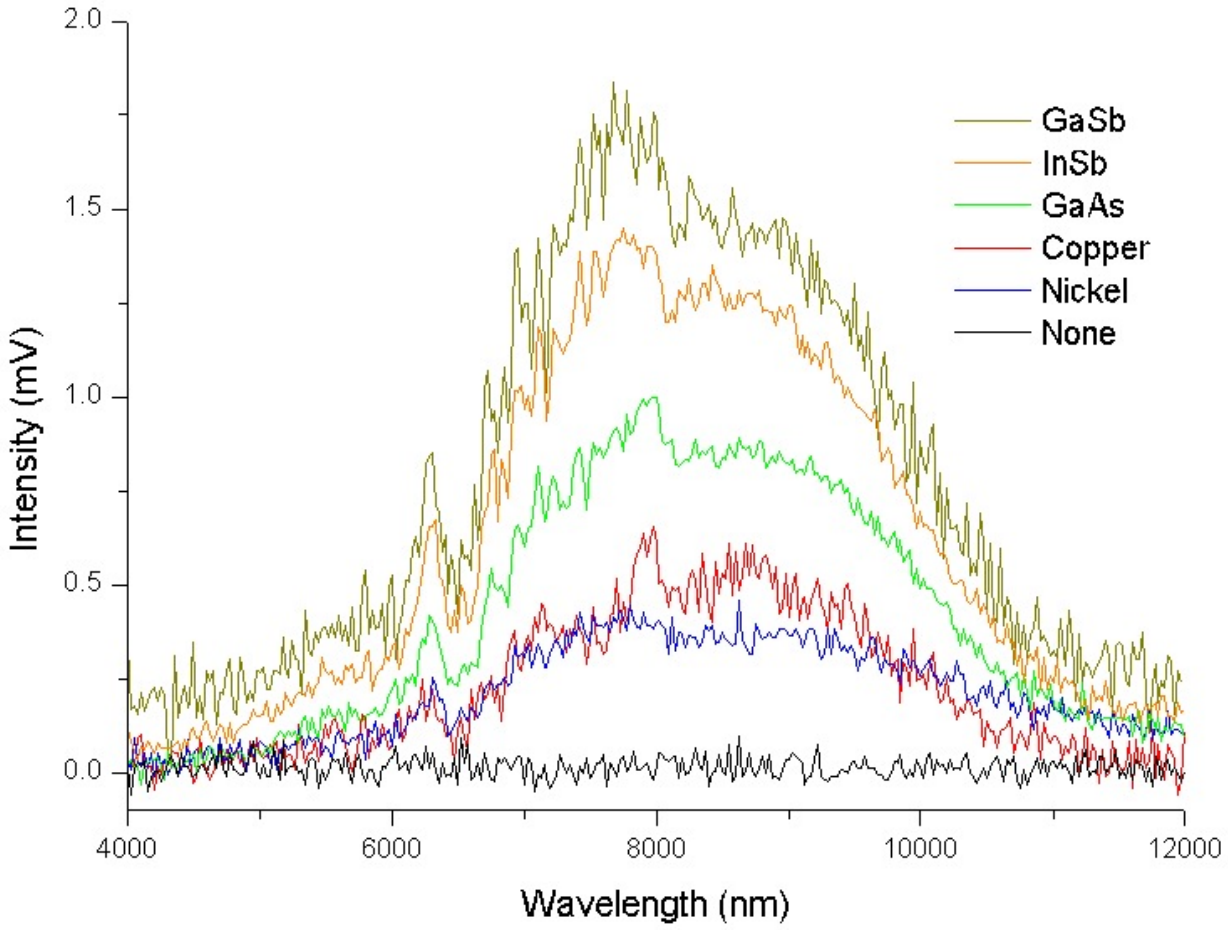

Figure 3.3. Comparison of absorption by different wafers and sample holders.

Quartz and sapphire

Quartz typically has about 90% transmissivity between 0.15 and 4.5 μm, depending on the kind of quartz, while sapphire has about 85% transmissivity between about 0.1 and 7μm. More important however, is that they have theoretically zero transmissivity elsewhere. The point where the transmissivity curve drops off sharply to zero defines that absorption edge. Thus, these materials should absorb infrared radiation coming from the sample holders with wavelengths longer than about 4 microns. We used quartz for initial testing, because it is what we had available. However, sapphire has better thermal conductivity than quartz, so the sample should get colder on top of sapphire than it will on top of quartz. Transmittance curves for fused quartz are shown in Figure

3.4. The difference between the curve labeled “124” and the curves labeled “214’ and “219” is the thickness of the quartz. The “124” curve was 10 mm, while the others were 1 mm. From these data, it appears that the wavelength at which the transmission drops off decreases with thickness. Transmittance for various materials are shown in Figure 3.5. From these data, it appears that the quartz transmittance decreases to zero above 4 μm, while sapphire does not drop to zero transmission until 7 μm.

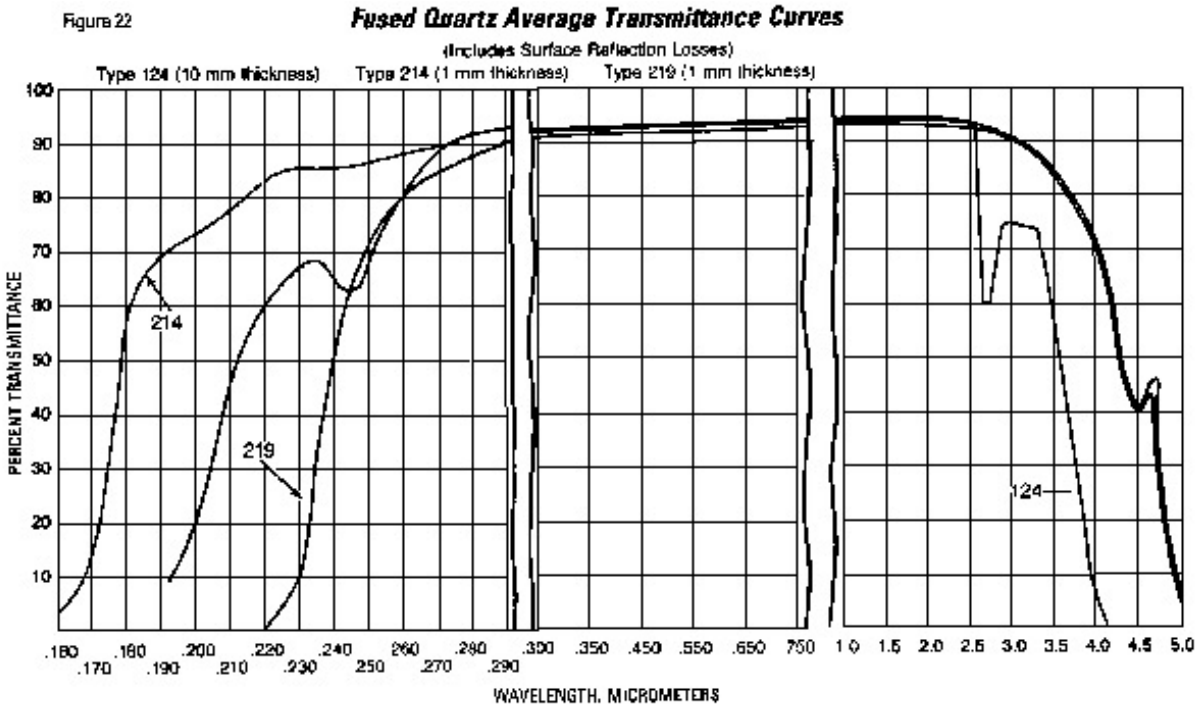

Figure 3.4. Transmittance curves for fused quartz.[16]

Initial testing showed that the quartz did not effectively absorb all of the radiation longer than 8 μm. It did absorb about 2/3 of it between about 8.2 and 9.4 μm, but then amplified the 8 μm, more so even than GaSb. From Figure 3.4, it appears that the absorption edge is dependent on thickness. The thicknesses shown in the figure are 10 mm and 1 mm, respectively. However, the spectra shown in Figure 3.6 depict that the absorption edge does not change with thickness. The first spectrum in Figure 3.6 corresponds to a single 3.5 mm-thick quartz wafer inside the shroud

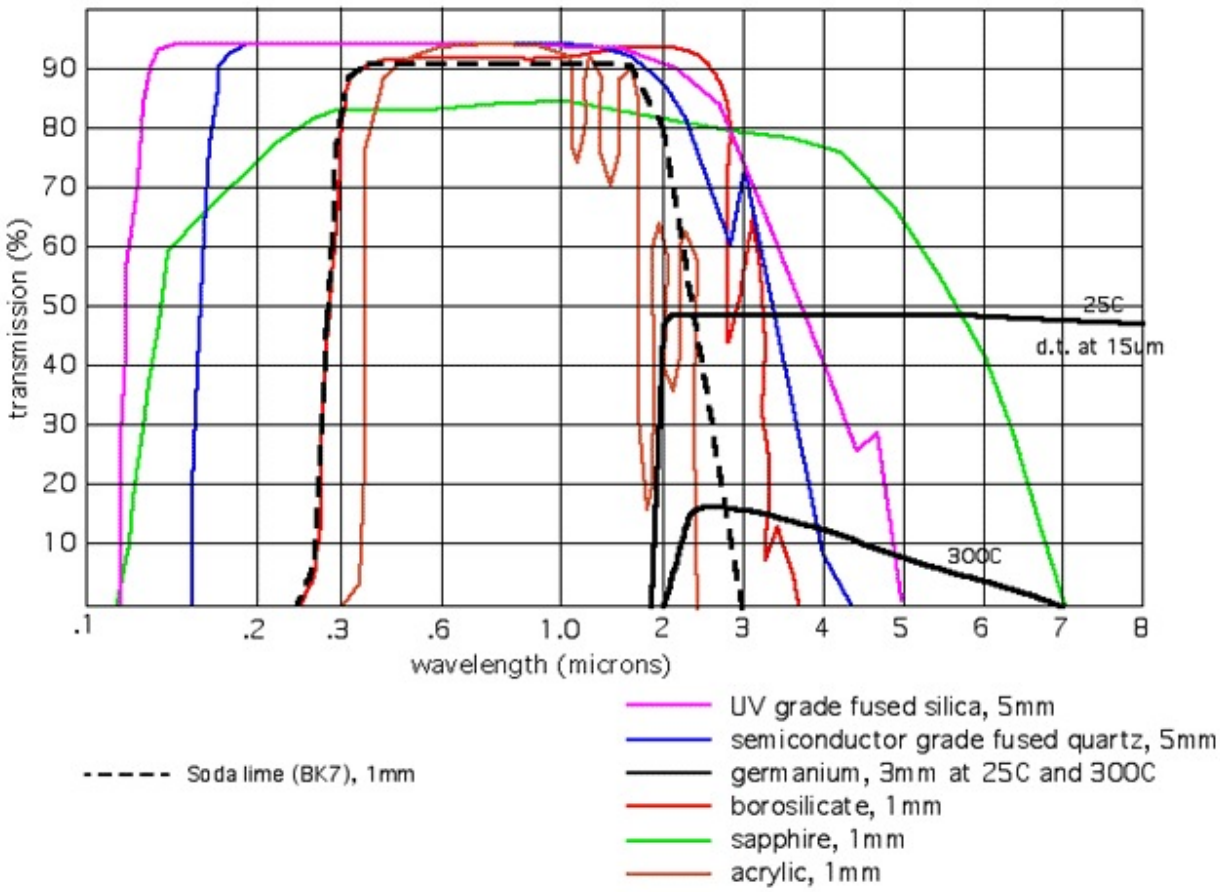

Figure 3.5. Transmittance curves for various materials.[17]

and therefore cooled to 10 K. The second spectrum corresponds to three quarts wafers stacked, bringing the effective thickness to 1.05 mm, still inside the shroud and therefore cooled to 10 K. The third spectrum corresponds to a large 3.5 mm-thick wafer held in front of the shroud, on the outside, and therefore at room temperature. The temperature dependence of the absorption by 1.05 mm-thick quartz at successively higher temperatures, starting at 10 K and warming up to 320 K, is shown in Figure 3.7. It can be seen from this plot that the width of the region of the original copper peak that is being absorbed by the quartz is narrow and unchanged by temperature, between about 8.2 and 9.4 μm. The intensity of the peak decreases with temperature, as expected from the ideal blackbody law of energy.

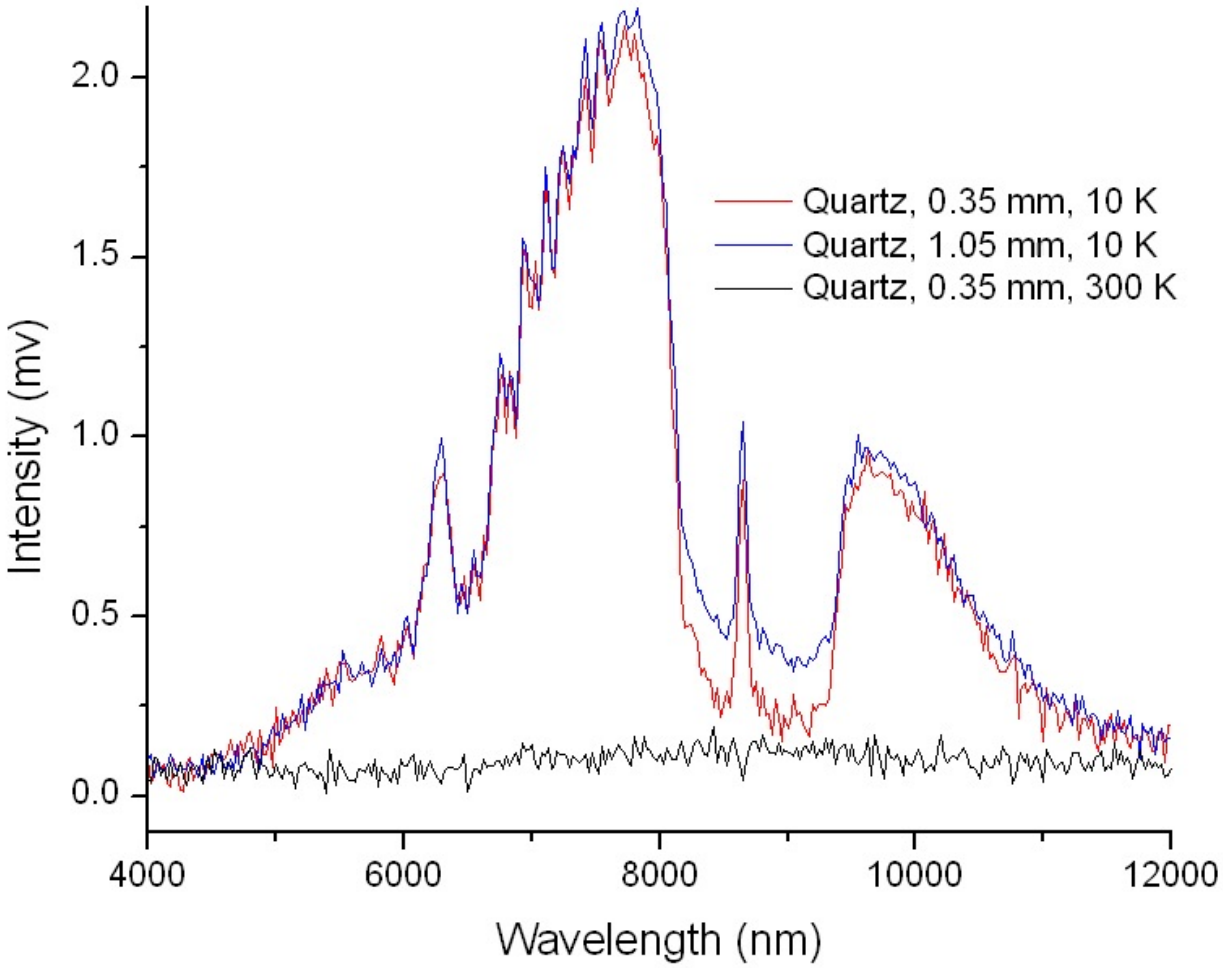

Figure 3.6. Comparison of absorption by different thicknesses of quartz wafers.

Chopper position

Many of the early problems that we faced in detecting a PL peak can be attributed to the position of the optical chopper. Initially, the chopper was positioned in front of the monochrometer, rather than in front of the laser, as shown in Figure 3.1. The lock-in amplifier requires modulation of the signal and it made sense to modulate the radiation directly entering the monochrometer for this purpose. However, it turned out that the sample holder itself also emitted some radiation, in the form of low-temperature, blackbody radiation. Much work was done to attempt to eliminate background radiation and blackbody radiation from the sample holder. By simply moving the chopper in front of the laser, the only radiation that becomes modulated at the right frequency for

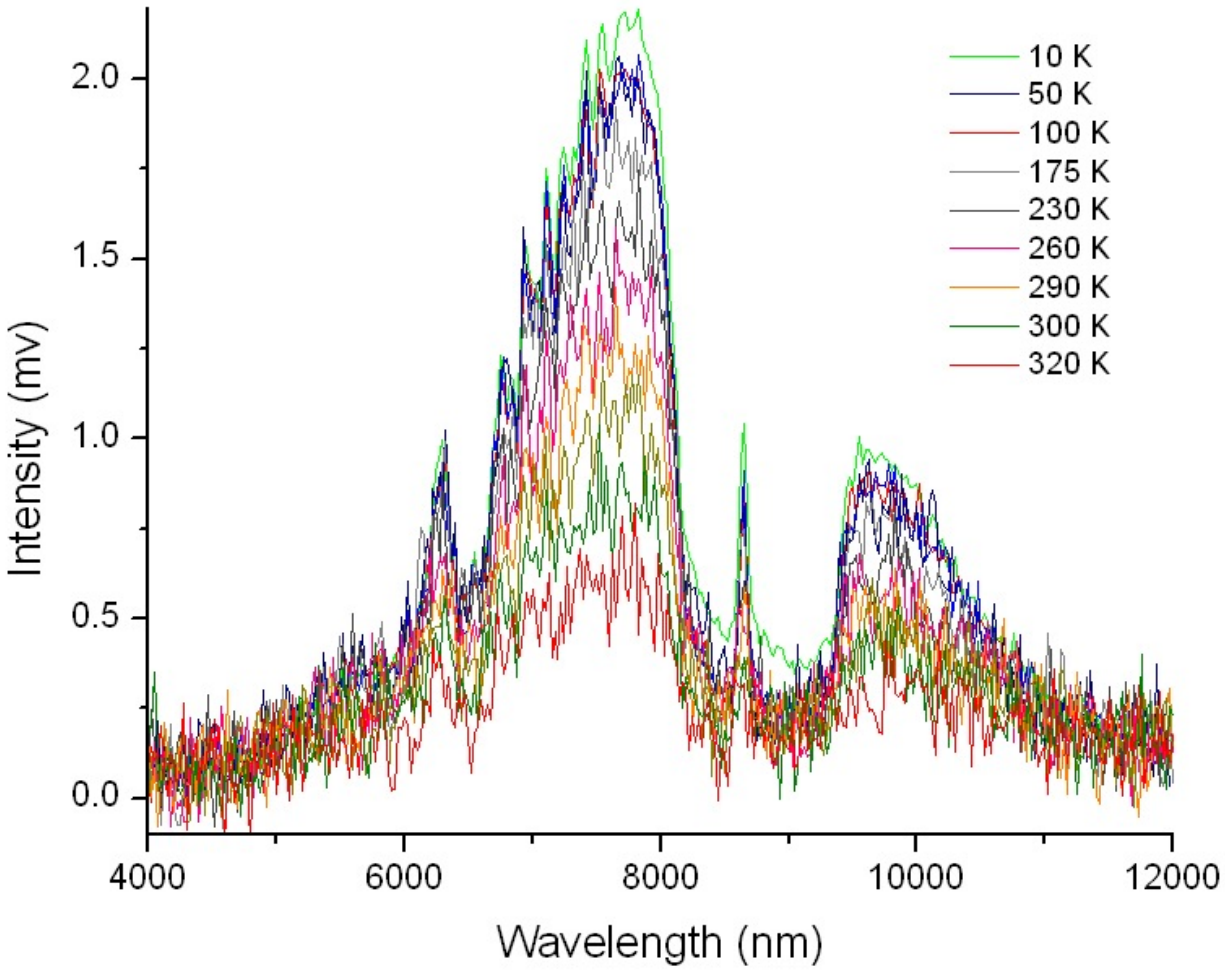

Figure 3.7. Temperature dependence of 1.05 mm-thick quartz.

the lock-in amplifier is the radiation that is caused by the laser exciting the sample. This effectively canceled all blackbody radiation. Even still, it was useful and interesting to learn about the effects of blackbody radiation, sample holders and absorption in a PL system. With the blackbody radiation from the sample holder eliminated, we began with an InSb bulk substrate and found that, while there was no broad, blackbody peak at 8 μm, there was no peak anywhere in the spectrum. The next problem turned out to be the type of laser that we were using.

Lasers

The first laser used was a 35 mW red HeNe laser that we already had in the lab. We found that a higher laser power was needed. Increase in PL intensity with increased laser power has been demonstrated for InSb[18], as shown in Figure 3.8. To keep the costs of new lasers to a minimum, small laser pointer models were chosen rather than large lasers designed for lab use. A drawback of these models, however, is that they typically are manufactured without an integrated power supply, relying instead on rechargeable batteries. This posed a problem, because as the batteries began to die, the PL intensity was drastically affected. It seemed that there were two states of laser intensity when powered with batteries: high power and low power, as shown in Figure 3.9. We did attempt to power the laser pointers with a DC voltage source connected in series with a 3 Ω resistor set to the voltage measured from a fully charged battery with a multimeter, but the intensity of the laser was diminished. Although the same current was being supplied to the laser with the DC source as was supplied by the battery, the intensity was much lower with the DC source. We did not want to increase the current further, risking the chance of burning out the laser. The second laser that we used to try to find a PL peak was a 1000 mW, blue diode laser. This laser was actually used in another project in the lab so we had it readily available, although it was slightly higher intensity than ideal for PL. We shown the blue laser on an InSb bulk substrate cooled to 10 K and recorded the spectrum. For the first time, we found a PL peak. Turning the laser off made the peak disappear. The InSb PL peaks that we found are presented in Chapter 4. The only problem with this system, was that the intensity of the blue laser was so high, that it was burning holes in the samples. PL is, by definition, a non-destructive characterization method. Our PL system was optically characterizing the material, but destructively. The third laser that we used was a 800 mW infrared diode laser. The PL peak persisted with this laser and it did not appear to have any

damaging effects to the surface of the samples. Another problem that can sometimes be caused by the laser is the presence of Fraunhofer diffraction from the laser entering the monochrometer slit, as shown in Figure 3.10. This is only a problem for the GaSb detector, because the other detectors have a filter for limiting the detection of light from the laser. A GaAs wafer can be used as a filter to block the scattered laser light[19]. In the future, the Fraunhofer fringes should be eliminated by focusing the laser beam through a pinhole and then collimated (expanded) again before illuminating the sample, in a lens-pinhole-lens configuration.

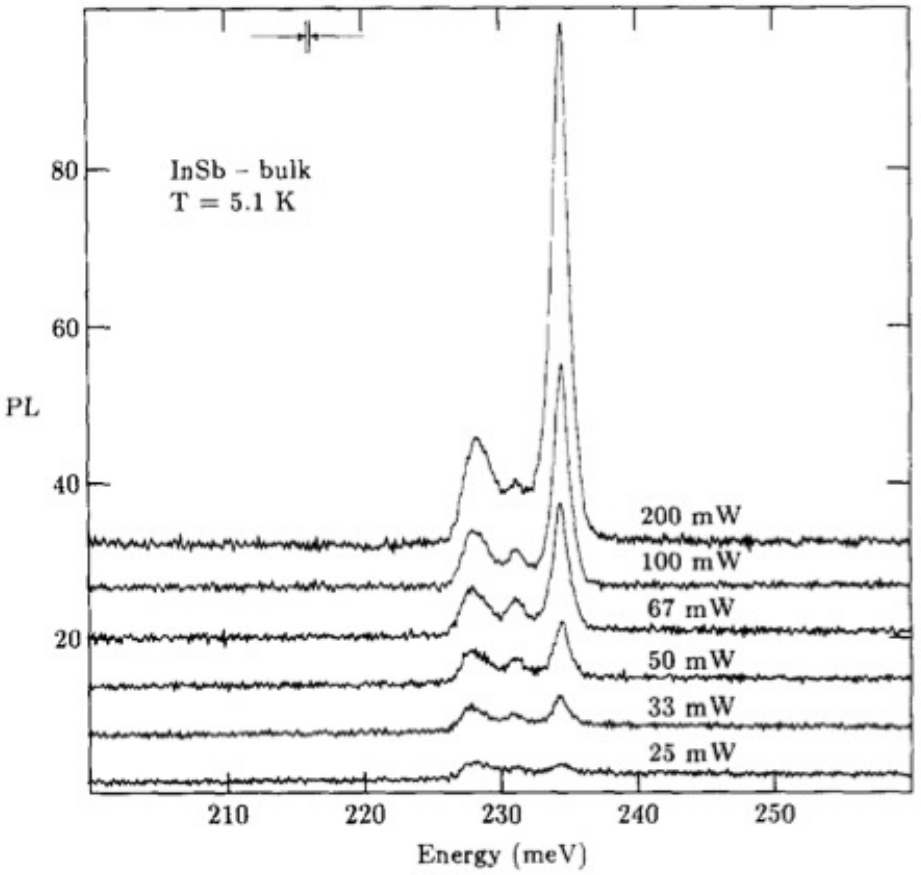

Figure 3.8. PL peaks for different laser intensities[18].

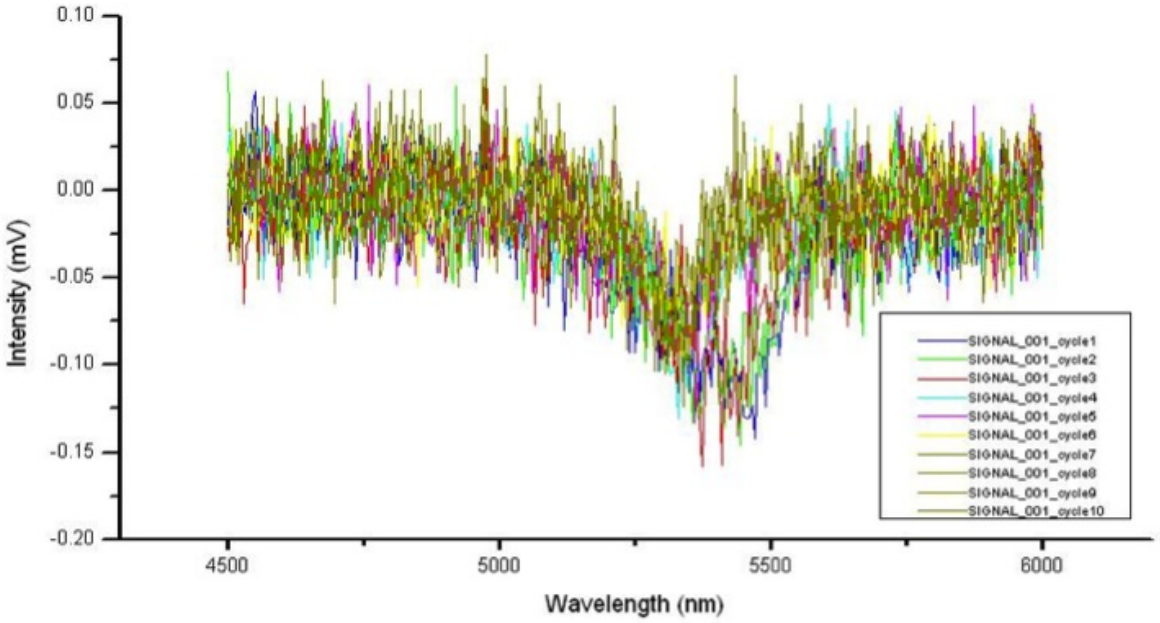

Figure 3.9. Effect of laser battery power.

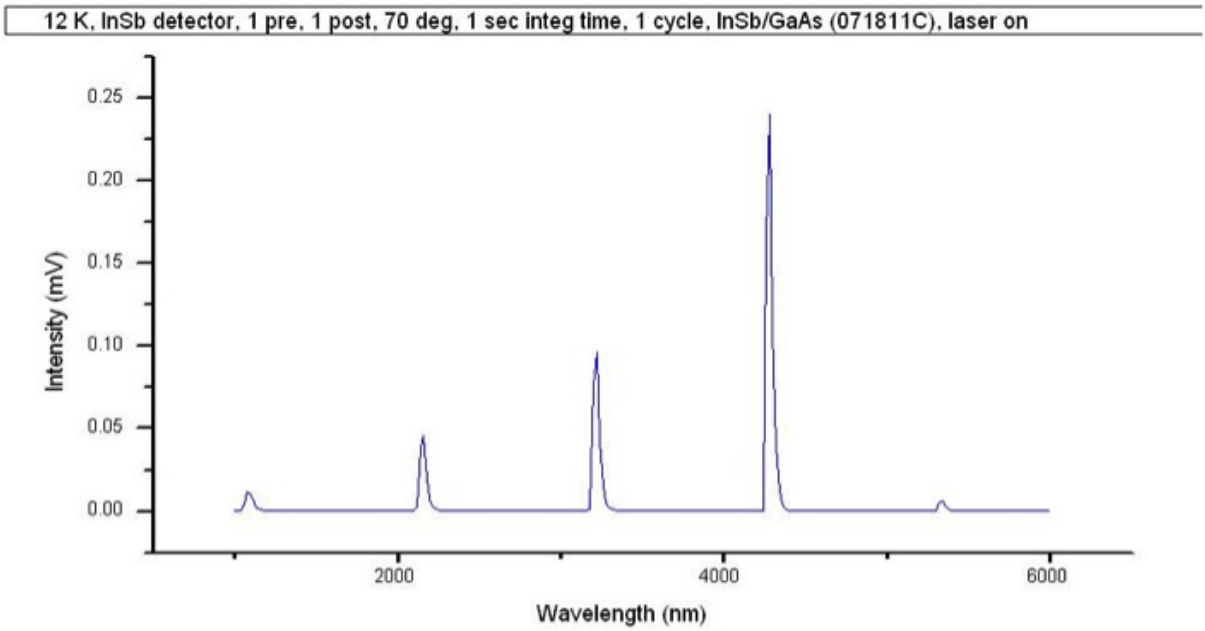

Figure 3.10. Fraunhofer fringes evident without the use of a filter.

LWIR

In the effort of preparing this system for detecting PL peaks in the LWIR region, we needed to procure a detector capable of detecting IR waves longer than 12 μm. Hamamatsu made a very good dewar-type IR detector, but only a "side-on" type dewar, rather than "head-on" as our existing monochrometer adapter requires. However, Hamamatsu was able to make a custom detector, as shown in Figure 3.11, to fit our needs. Additionally, a new grating was ordered for the monochrometer from Horiba, for the 12-20 μm range.

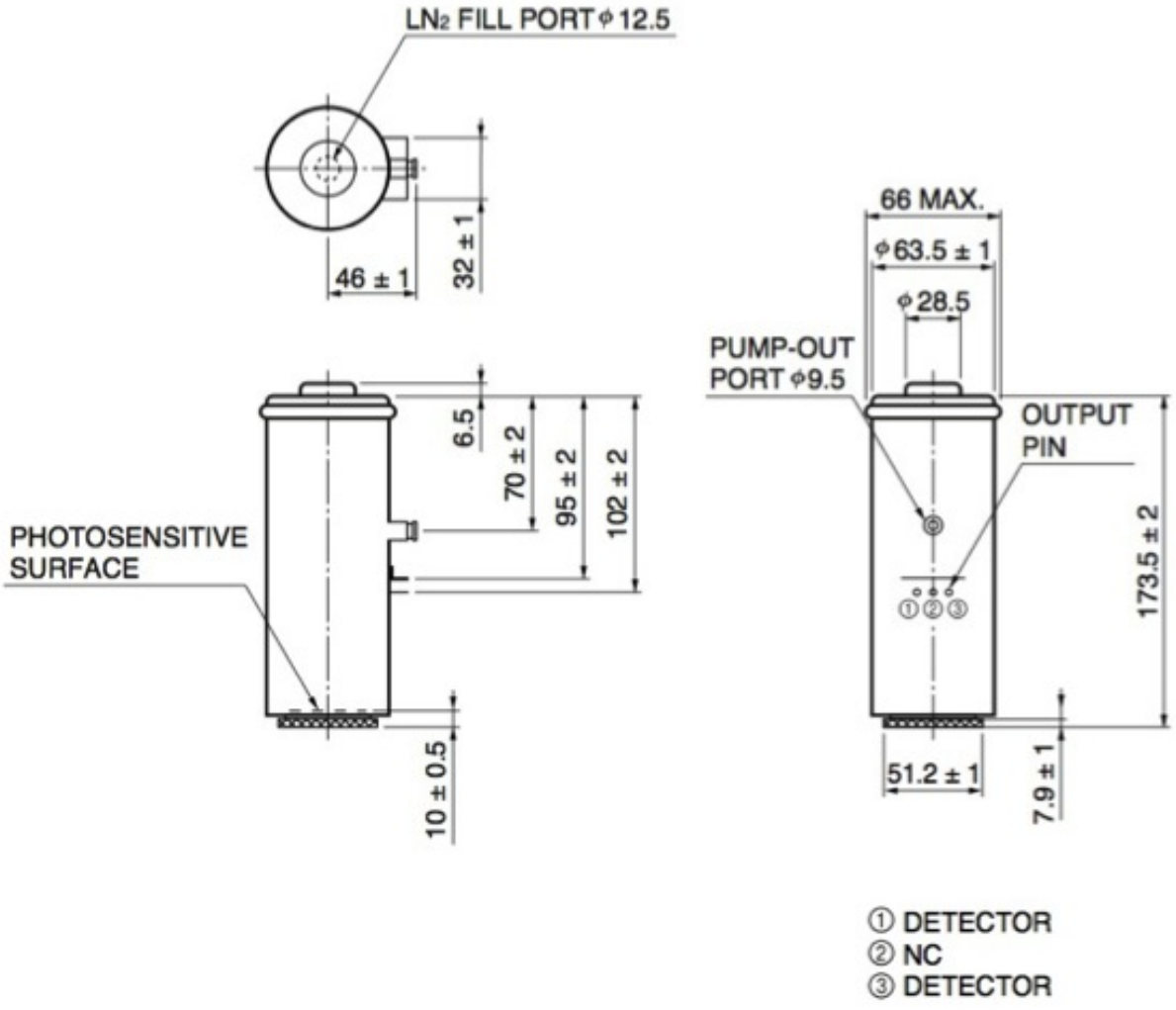

Figure 3.11. Custom detector from Hamamatsu to fit our monochrometer adapter.

Photolithography

The process of photolithography is used to fabricate a photodetector device from the semiconductor film. The sample is coated with a chemical photoresist and placed into a machine called a mask aligner. A photomask is aligned on top of the sample and ultraviolet (UV) light is shown onto the sample, as shown in Figure 3.12. The photomask prevents the light from reacting with some areas of the photoresist, while exposing it in other areas. Positive-type photoresist is removed when exposed to UV, while negative-type is not. When the sample is later subjected to chemical etching, the regions of the film not protected by photoresist will be etched away at a rate dependent on the type of etchant used. In this way, sections of the film can be removed to expose the bulk substrate underneath or even specific layers in between.

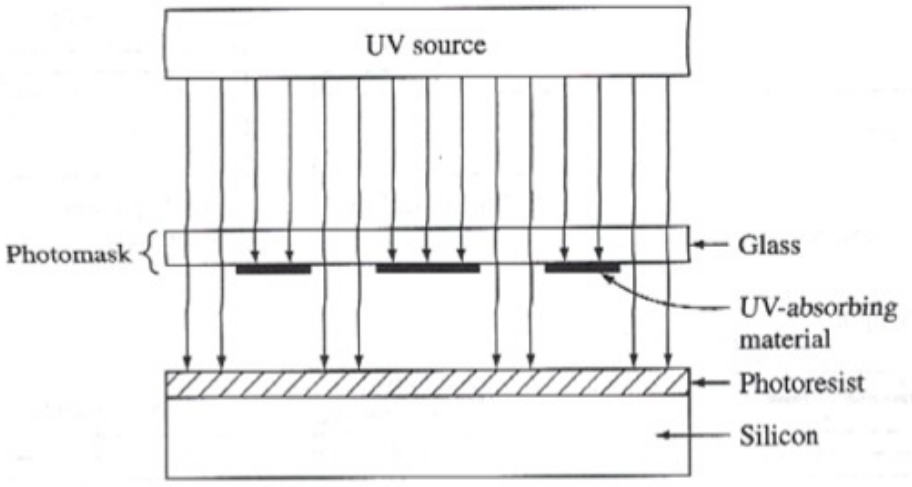

Figure 3.12. Cross-sectional diagram showing the process of photolithography[20].

One type of photodetector is called a P-I-N photodetector, in which there are three layers grown on top of the substrate: first a layer doped with more electrons than holes (n-type), then an un-doped layer (intrinsic), and finally a layer doped with more holes than electrons (p-type). The device is created by etching a portion of the film down to the p-type layer, removing the n-type

and intrinsic layers in that portion. A gold bond contact is then placed on the exposed p-type layer and another contact is placed on the top of the film, on the n-type region. A photomask was designed as shown in Figure 3.13. To minimize the foundry-costs associated with using multiple photomasks, a process of rotation was devised such that all of the steps necessary for the complete lithographic processes could be completed with a single photomask. This is accomplished by successive 90^{o} rotations. The three sections of vertical bars in the center region of the photomask was part of a project done by another student, for transmission line measurements not associated with photodetector device fabrication. The parts used for fabricating a photomask are the four sections along the outside edges of the mask. The strip all the way around the outer edge is used for alignment in the photolithography machine.

The sample can be held at a fixed spot in the photolithography machine while the photomask is used at one orientation and then rotated by 90^{o} for the next step in the process. The steps of the process are shown in Figure 3.14. The portion of the mask used first is that shown at the bottom of the mask in Figure 3.13. Moving downwards from the top of Figure 3.14 (a), the mask feature to be used is shown, followed by a side-on view of the as-grown film layers. This mask feature covers a corner of the film, preventing it from being exposed to UV radiation. By having coated the film with negative photoresist, only the parts exposed to UV will remain, indicated by the next step down in Figure 3.14 (a). Finally, the sample is etched down to the n-type layer in the section where the photoresist has been removed, shown in the final step. Then, the film can be recoated with photoresist and the photomask rotated 90^{o}. Again, negative photoresist is used, such that the regions of the film covered by the mask feature shown at the top of Figure 3.14 (b) will retain the photoresist when UV light is shown onto the film (next image down in Figure 3.14 (b)). Instead of removing layers of the film, as before, now we want to deposit insulating regions

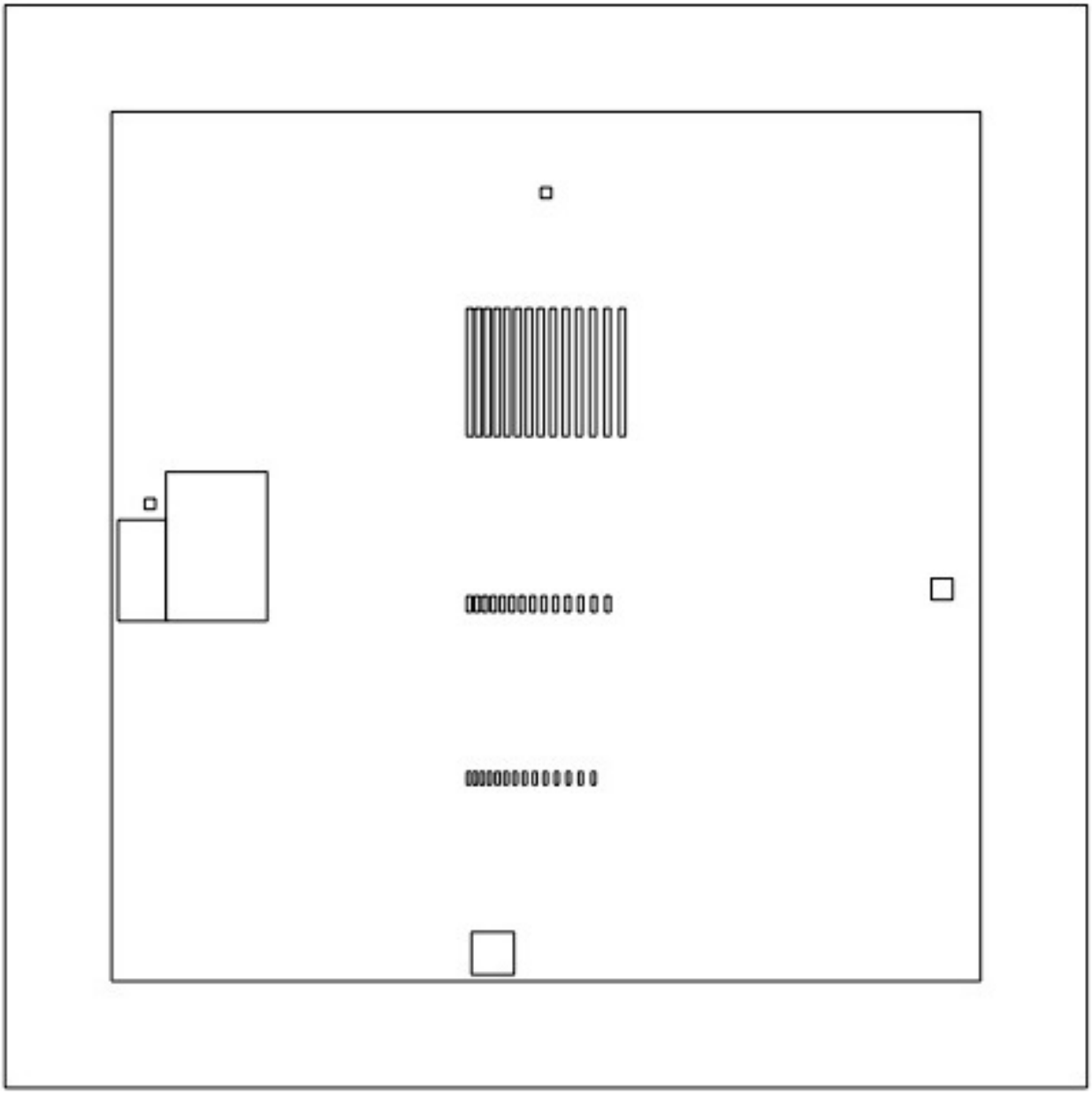

Figure 3.13. Photomask designed for photodetector device.

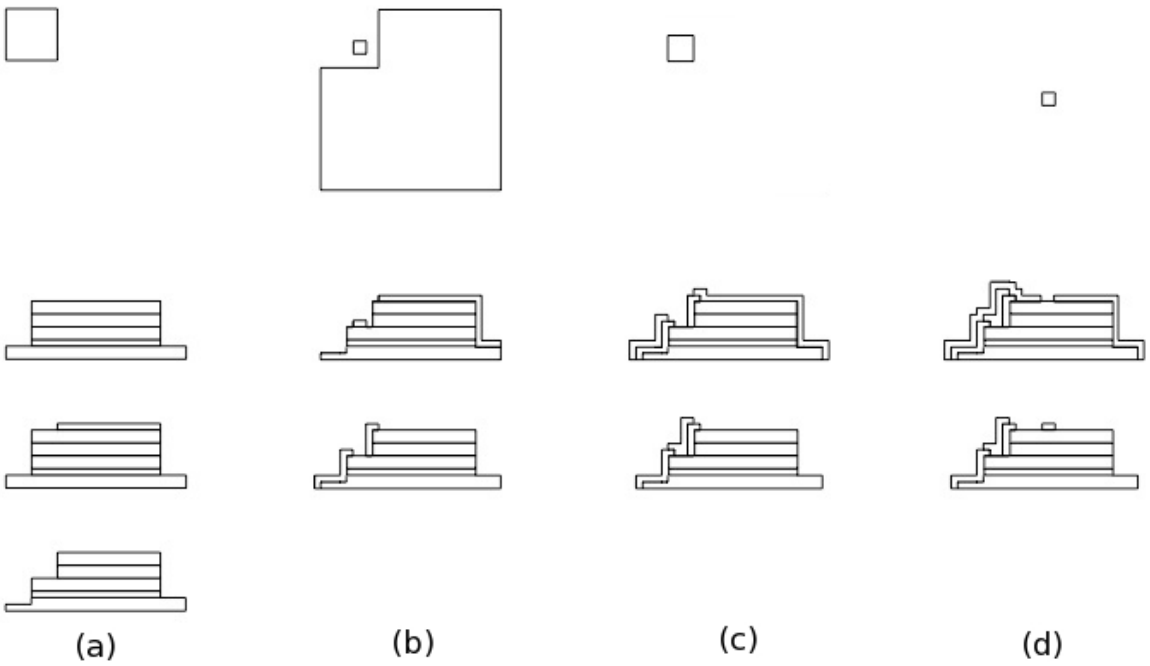

Figure 3.14. Process of photolithography for photodetector device.

onto the film for placing electrodes. This is done by the process of electron beam evaporation. The insulative material deposited will not adhere to the regions of the film with photoresist, as shown at the bottom of Figure 3.14 (b). The two layers of deposited insulative material shown allow placement of a conductive material that is only in contact with the n-type layer, while insulated from the other layers.

To deposit the conductive material, electron beam evaporation is again used, but this time positive photoresist is used, such that only the regions of the film not protected by the mask feature shown at the top of Figure 3.14 (c) will retain photoresist, as shown in the next image down. The mask has now been rotated 180^{o} from its original position. Again, the deposited conductive material will not adhere to the photoresist in the electron beam evaporation, leaving the conductive material insulated from all other layers except the n-type layer, as shown at the bottom of Figure

3.14 (c). Now, an electrode can be placed on top of the conductive material using a gold-bonding machine and a gold wire attached to it. We also want to place a second electrode, for the p-type layer. This can be done with positive photoresist and the photomask feature shown at the top of Figure 3.14 (d), after having now rotated the photomask 270^{o} from its original position. The positive photoresist must protect the entire film from the final evaporation of conductive material, except for a small region at the center of the surface of the film, as shown in the next image down. Finally, the bottom image in Figure 3.14 (d) shows the result of photolithography for this photodetector device. A second gold-bond contact is placed on this final electrode. This process can also be visualized in Figure 3.15.

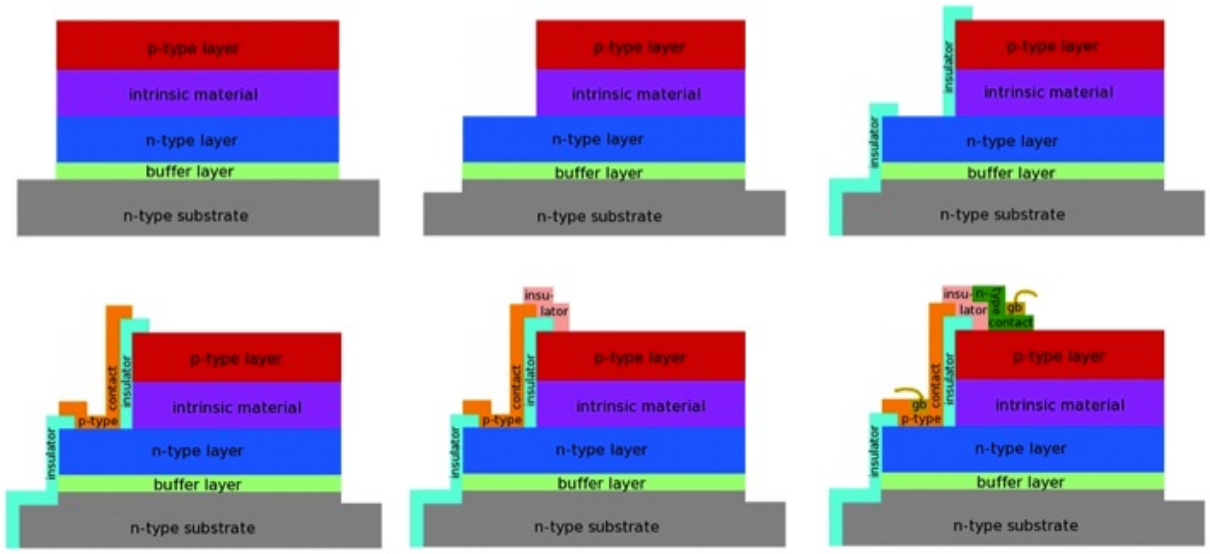

Figure 3.15. Process of photolithography for photodetector device.

Photoconductivity

Photoconductivity is a characterization method at the device level, by which a photodetector's change in conductivity upon optical illumination may be measured. For example, in a

uniform p-type semiconductor that is being uniformly illuminated optically[20], the electron and hole carrier concentrations, n and p, deviate from their thermal equilibrium values, n_0 and p_0, by the excess carrier concentrations, δ_n and δ_p, respectively, due to the optical excitation

$$\begin{aligned} n &= n_0 + \delta_n \\ p &= p_0 + \delta_p \end{aligned} \tag{3.3}$$

Since $p_0 \gg n_0$ in an extrinsic p-type semiconductor, the net thermal recombination rate may be written as

$$R_n^{\text{net}} = \frac{\delta n}{\tau_n} \tag{3.4}$$

where the low-level injection condition, δn, $\delta p \ll p_0$, is assumed. Then, the electron concentration will satisfy the rate equation

$$\frac{\partial n}{\partial t} n = G_0 - \frac{\delta n}{\tau_n} \tag{3.5}$$

where G_0 is the net optical generation rate. For a uniform semiconductor with a dc voltage bias V, the electron and hole current densities may be given by only the drift components, since there is no diffusion current due to the lack of spatial dependence $\left(\frac{\partial}{\partial x} = 0\right)$

$$\begin{aligned} J_n &= q\mu_n nE \\ J_p &= q\mu_p pE \end{aligned} \tag{3.6}$$

The total current density is

$$J = J_n + J_p = q\left(\mu_n n + \mu_p p\right) E = \sigma E \tag{3.7}$$

where the conductivity is

$$\sigma = q\left(\mu_n n + \mu_p p\right) \tag{3.8}$$

The photoconductivity, $\Delta\sigma$, is defined as the difference between the conductivity when there is an optical injection and the dark conductivity, σ_0,

$$\begin{aligned} \Delta\sigma &= \sigma - \sigma_0 = q\left(\mu_n \delta n + \mu_p \delta p\right) \quad (3.9) \\ \sigma_0 &= q\left(\mu_n n_0 + \mu_p p_0\right) \quad (3.10) \end{aligned}$$

The total current, I, is the current density, J, multiplied by the cross-sectional area of the semiconductor,

$$\begin{aligned} A &= wd \\ I &= JA = \sigma E A = \frac{\sigma A V}{l} \quad (3.11) \end{aligned}$$

where the electric field, $E = \frac{V}{l}$, where l is the length of the sample. The photocurrent, ΔI is defined as the difference between the total current in the presence of optical excitation and the dark current,

$$\begin{aligned} I_0 &= \frac{\sigma_0 A V}{l} \\ \Delta I &= I - I_0 = \Delta\sigma \frac{A}{l} V = q\left(\mu_n \delta n + \mu_p \delta p\right) \frac{A}{l} V \quad (3.12) \end{aligned}$$

One of the two remaining ports of the Horiba iHR-320 monochrometer can be used for mounting an infrared source, as shown in Figure 3.16, to use this system for measuring photoconductivity at the device level. The chopper is moved back in front of the monochrometer, to modulate the IR photons being radiated through the monochrometer towards the sample. The IR photons are reflected by the mirrors onto the surface of a photodetector device and the photocurrent

is measured by connecting the lock-in amplifier to gold-bond contacts attached to the device. The device is mounted on the same sample holder and position as was used for photoluminescence, but now without the shroud attached or the cryopump running, so the sample is at room temperature. Although the characterization system and photolithography process is ready for a photodetector device, a failure in the equipment used to grow the film used for fabricating the device prevented testing of the device-level characterization aspect of the system developed in this thesis.

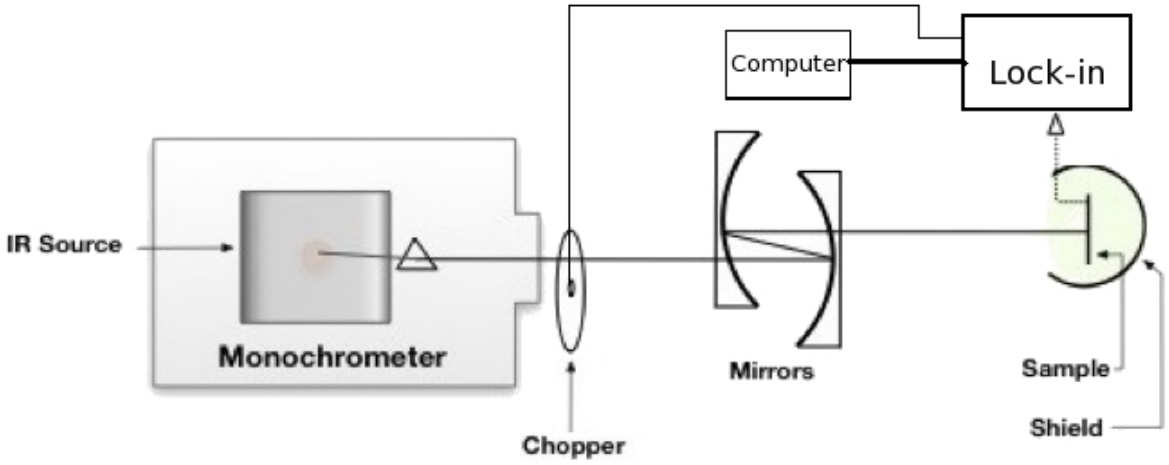

Figure 3.16. Schematic setup of the photoconductivity experiment.

CHAPTER 4

Results and Discussion

The energy gap of a bulk InSb substrate was calculated using equation 2.14, for $a = 6.45$ $\mathring{A}$, $b = d - a$, and a V_o of 70 eV. The energy gap of InSb was predicted to be 0.2 eV. From equation 3.1, this corresponds to a wavelength of 5.27 μm, which agrees with PL data collected for InSb and with published values. A Matlab program was written to implement this calculation, shown in the Appendix. We successfully measured the PL emission of a bulk InSb substrate using the system developed for this thesis. The PL peak is centered at about 5.2 $\pm$ 0.1 μm, shown in Figure 4.1. This agrees with the InSb peak wavelength reported by others[18, 19, 21]. This first peak was measured using the InSb detector and with grating #3. The intensity of the peak is about 27 μV and there is very little noise in the spectrum. Initially, the PL peak when switching to the MCT detector was buried in noise. But by fine-tuning the lock-in settings, we were able to obtain the PL signal shown in Figure 4.2 with the MCT detector for the InSb substrate. The lock-in settings used were 1 second pre-processing time constant, 1 second post-processing time constant, 200 μV sensitivity, and a 70^o phase. Grating #2 was then used in measuring the PL of the InSb substrate, shown in Figure 4.3, again using the same lock-in settings as in Figure 4.2. The InSb PL measured using the MCT detector and grating #3 is shown in Figure 4.4 and using the InSb detector and grating #2 is shown in Figure 4.5. It can be seen that the noise and strength of the PL peak depends greatly on the type of detector used, the grating used, and the lock-in settings. Future development of this system will require experimentation to determine how to optimize the PL signal. Other ways to

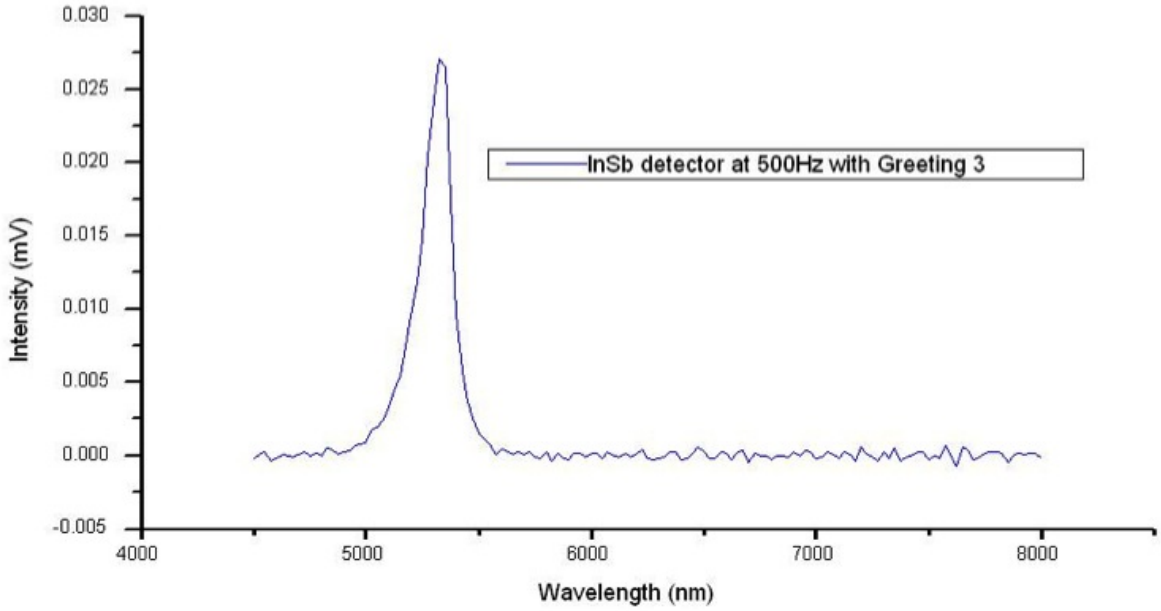

Figure 4.1. PL peak for InSb wafer using InSb detector and grating #3.

optimize the PL signal in the future are to improve the alignment of the optics in the system by (1) watching the lock-in output while fine-tuning the position of the mirrors and other optics and (2) looking at the infrared back-reflectance from the monochrometer slit and pinhole lenses using an IR-sensitive “laser card”, and adjusting optic positions accordingly.

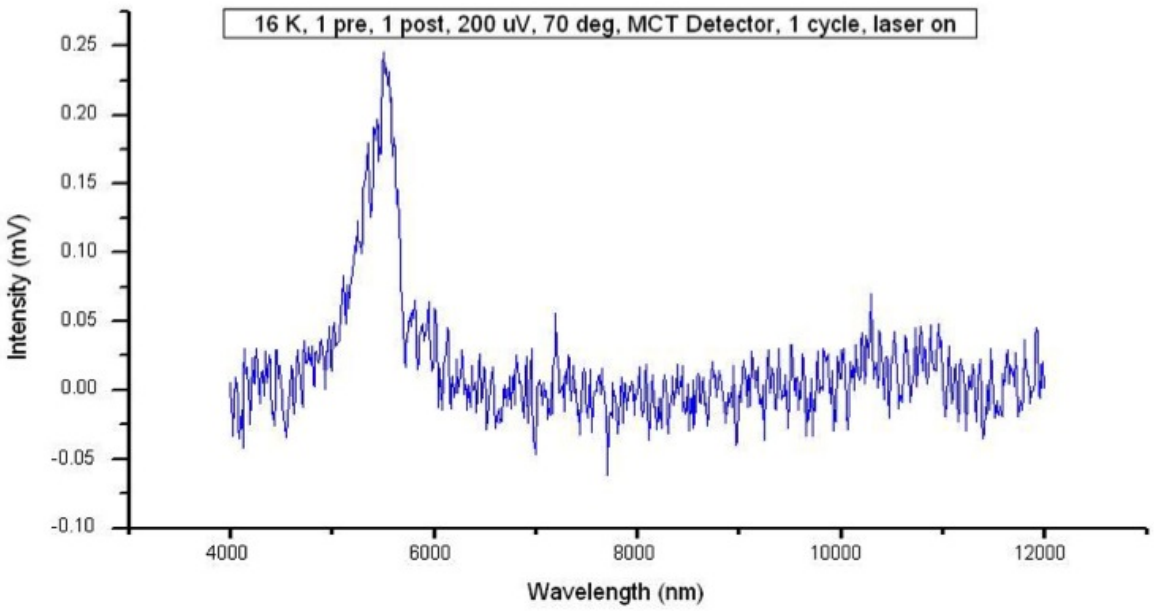

Figure 4.2. PL peak for MCT detector and grating #3.

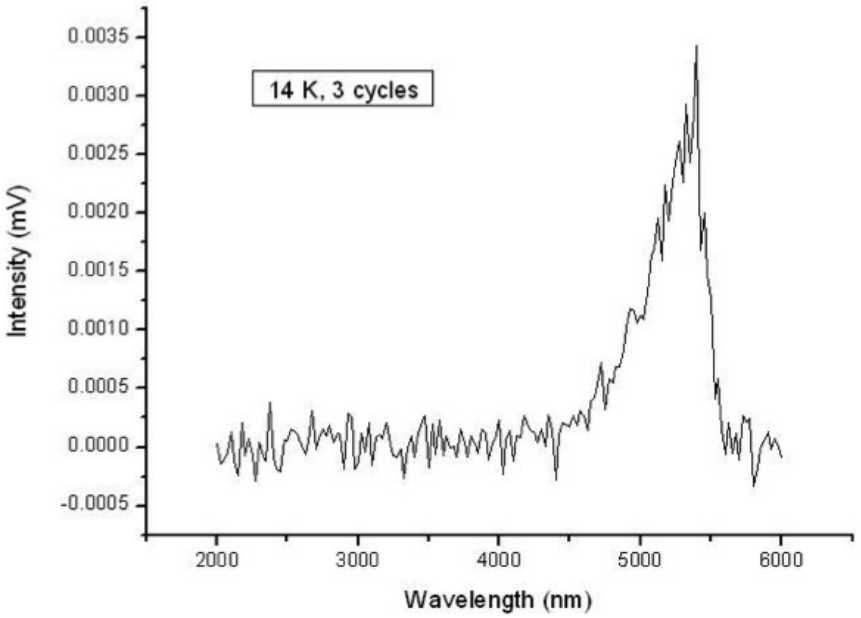

Figure 4.3. PL peak for MCT Detector and grating #2.

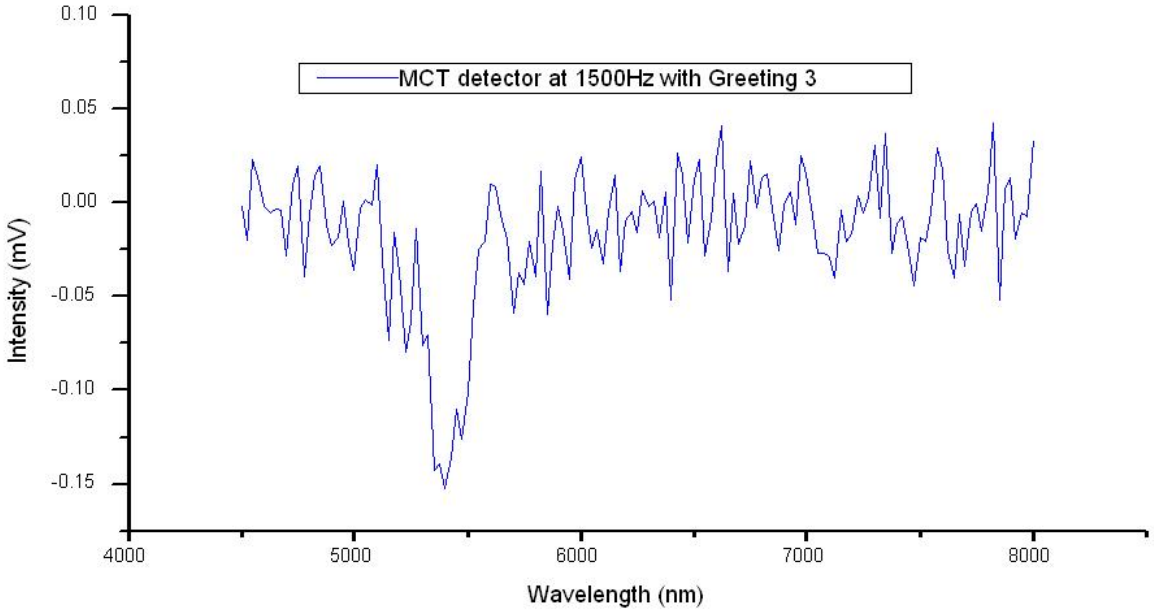

Figure 4.4. PL peak for MCT Detector and grating #3.

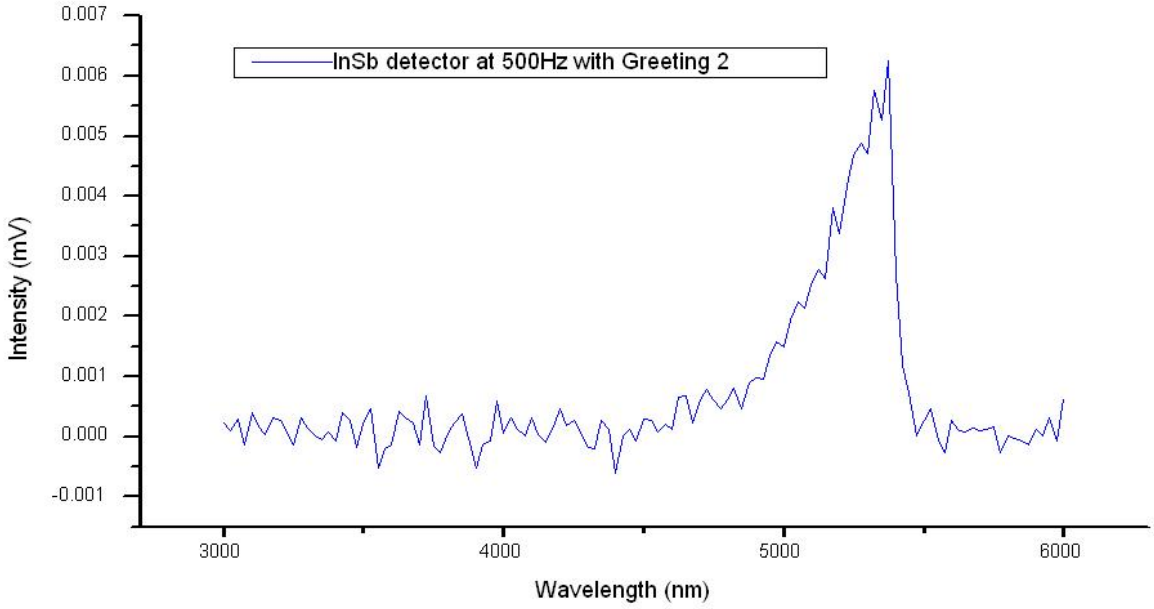

Figure 4.5. PL peak for InSb Detector and grating #2.

CHAPTER 5

Conclusions and Future Work

The energy gap of InSb was theoretically predicted to be 0.2 eV by using the Kronig-Penney model, which agrees with published values. The PL of a bulk InSb substrate was measured and a peak was found at 5.2 μm, which agrees with published PL data for InSb, and corresponds to an energy of 0.2 eV. The photodetector device fabrication process was setup and a system for measuring the photoconductivity of the device was developed, but the device itself was not fabricated due to growth-equipment failures. In the future, the theoretical model can be extended to accommodate a superlattice structure as discussed in Chapter 2 and the photoluminescence system can be improved by aligning the optics using techniques such as back-reflectance and using the lock-in more effectively, as well as eliminating the Fraunhofer effects by using a pinhole. The system for fabricating the photodetector device should be used when a PIN-type material is successfully grown and the planned photoconductivity system used to characterize that device.

References

[1] Razeghi, M. & Henini, M. (2002). *Handbook of Infrared Detection Technologies (2nd ed.)*. New York: Elsevier.

[2] Klocke, D. et al. (2011). Infrared receptors in pyrophilous ("fire loving") insects as model for new uncooled infrared sensors. *Beilstein Journal of Nanotechnology, 2,* 186.

[3] Mahulikar, S. P. et al. (2009). Infrared signature studies of aircraft and helicopters. *PIERS Proceedings.*

[4] Bandara, S. et al. (1998). Quantum well infrared photodetectors for long wavelength infrared applications. *SPIE Proceedings.*

[5] Kronig, R. de L. & Penney, W. G. (1931). Quantum mechanics of electrons in crystal lattices. *Proceedings of the Royal Society London A, 130,* 499.

[6] McQuarrie, D. A. (1996). The Kronig-Penney model: A single lecture illustrating the band structure of solids. *The Chemical Educator, 1,* 1.

[7] Harrison, P. (1999). *Quantum Wells, Wires and Dots (2nd ed.)*. West Sussex, UK: Wiley & Sons, Inc.

[8] Blakemore, J. S. (1974). *Solid State Physics (2nd ed.)*. Philadelphia: W. B. Saunders Co.

[9] Tinkham, M. (1964). *Group Theory and Quantum Mechanics*. New York: McGraw-Hill.

[10] Ioffe Physical Technical Institute (2011). Basic parameters of indium antimonide. *<http://www.ioffe.rssi.ru/SVA/NSM/Semicond/InSb/basic.html>*.

[11] Aguinaldo, R. (2008). Modeling solutions and simulations for advanced III-V photovoltaics based on nanostructures. *Rochester Institute of Technology, 130,* 499.

[12] Esaki, L. (1986). A bird's-eye view on the evolution of semiconductor superlattices and quantum wells. *Journal of Quantum Electronics, QE-22,* 1611.

[13] Allan, G. (1986). *Heterojunctions and semiconductor superlattices*. New York: Springer.

[14] Razeghi, M. (2009). *Fundamentals of Solid State Engineering (3rd ed.)*. New York: Springer.

[15] Omega Engineering (2011). Emissivity of some common materials. <*http://www.omega.com/literature/transactions/volume1/emissivitya.html*>.

[16] National Scientific Company (2011). Transmissivity of quartz. <*http://www.quartz.com/gedata.html*>.

[17] Rayotek Scientific (2011). Transmissivity of glass and sapphire. <*http://www.rayotek.com/technical_info_glass_sapphire.htm*>.

[18] Rowell, N. L. (1988). Infrared photoluminescence of intrinsic InSb. *Infrared Physics, 28.*

[19] Fang, Z. M. et al. (1990).Photoluminescence of InSb, InAs, and InAsSb grown by organometallic vapor phase epitaxy. *Journal of Applied Physics, 67,* 11.

[20] Chuang, S. L. (1995). *Physics of Optoelectronic Devices*. New York: John Wiley & Sons.

[21] Jin, S. et al. (2011). Sb antisite defects in InSb epilayers prepared by metalorganic chemical vapor deposition. *Journal of Crystal Growth, 318.*

APPENDIX

```
%This program calculated the band gap in eV using numerical solutions to
%the Kronig Penny model for a material

% written by Jon Poe
% modified by R Adelberger 9/24/11

function[]=kp()

% values of fundamental constants in eV, sec, Angstroms
h=4.135667e-15; % Plancks constant in eV-seconds.
hbar=h/(2*pi); % hbar
c=3e18; % speed of light in Angstroms/sec

%parameters for InSb
d=6.479; % lattice constant in Angstroms

display(strcat('Lattice constant =  ', num2str(d),' Angstroms'))

m0=0.511e6; % rest energy of electron
m=0.014*m0; % effective rest energy of electron in the substrate
```

```
% parameters needed for the Kronig Penny algorithm implimentation

dE=.0001; %spacing in epsilon in calculation of F

indicies = 0;  %initialize variable to count width of bandgap in epsilon
NoGap = 0;  % intitalize variable to make sure that F crosses -1)

a=input('Well width in Angstroms = ')  ; % well width (in Angstrom)

if a>d
    disp('Well width is larger than lattice spacing, Not possible')
    return
end
b=d-a; % barrier width (Angstroms)

%inputting the variables for the KP model
Vo=input('Well depth in eV = '); % potential height

A=a*sqrt(((2*m)/((hbar*c)^2))*Vo);
r=b/a;

% make a vector containing all values of epsilon
epsilon=[.0001:dE:.9999];
```

```
% calculating the F function from Equation 2.14 in Thesis of Jon Poe
F=((1-2.*epsilon)./(2.*epsilon.^(0.5).*(1-epsilon).^(0.5))).*sinh(...
        r.*A.*(1-epsilon).^(0.5)).*sin(A.*epsilon.^(0.5))+cosh(...
        r.*A.*(1-epsilon).^(0.5)).*cos(A.*epsilon.^(0.5));

%finding the number of time a value of epsilon makes F<1 ... not allowed
%state
for l=1:length(F)
   if F(l)<-1
      indicies=[indicies,l];
      NoGap = 1;
   end

end

%model does not give an energy gap if F never gets >-1
if F(l)<-1
    disp('No band gap for these parameters')
    return
end
```

```
% model does not give an energy gap if F never gets to -1
if NoGap < 1
    disp ('No band gap for these parameters')
    return
end
EnergyGap = length(indicies)*dE*Vo;
EG= num2str(EnergyGap);

FigTitle = strcat('Energy gap = ', EG , ' eV');

display(strcat('Energy gap = ', EG , ' eV'));
FigTitle2= strcat('Lattice constant = ', num2str(d),...
        'Angs ..  Well width = ', num2str(a),...
        ' Angs .. Well depth = ', num2str(Vo), 'eV');

figure;
plot(epsilon,F);
ylabel('F(\epsilon)');
xlabel('\epsilon');
axis([0 1 -1 1]);
title({FigTitle,FigTitle2} );
print -djpeg -r300 'plot.jpg'
```

```
end
```